

Eat-Radar: Continuous Fine-Grained Eating Gesture Detection Using FMCW Radar and 3D Temporal Convolutional Network

Chunzhuo Wang, T. Sunil Kumar, Walter De Raedt, Guido Camps, Hans Hallez, Bart Vanrumste

arXiv:2211.04253v1 [cs.CV] 8 Nov 2022

Abstract—Unhealthy dietary habits are considered as the primary cause of multiple chronic diseases such as obesity and diabetes. The automatic food intake monitoring system has the potential to improve the quality of life (QoF) of people with dietary related diseases through dietary assessment. In this work, we propose a novel contact-less radar-based food intake monitoring approach. Specifically, a Frequency Modulated Continuous Wave (FMCW) radar sensor is employed to recognize fine-grained eating and drinking gestures. The fine-grained eating/drinking gesture contains a series of movement from raising the hand to the mouth until putting away the hand from the mouth. A 3D temporal convolutional network (3D-TCN) is developed to detect and segment eating and drinking gestures in meal sessions by processing the Range-Doppler Cube (RD Cube). Unlike previous radar-based research, this work collects data in continuous meal sessions. We create a public dataset that contains 48 meal sessions (3121 eating gestures and 608 drinking gestures) from 48 participants with a total duration of 783 minutes. Four eating styles (fork & knife, chopsticks, spoon, hand) are included in this dataset. To validate the performance of the proposed approach, 8-fold cross validation method is applied. Experimental results show that our proposed 3D-TCN outperforms the model that combines a convolutional neural network and a long-short-term-memory network (CNN-LSTM), and also the CNN-Bidirectional LSTM model (CNN-BiLSTM) in eating and drinking gesture detection. The 3D-TCN model achieves a segmental F1-score of 0.887 and 0.844 for eating and drinking gestures, respectively. The results of the proposed approach indicate the feasibility of using radar for fine-grained eating and drinking gesture detection and segmentation in meal sessions.

Index Terms—FMCW radar, human activity recognition, food intake monitoring, eating gesture detection, deep learning.

1 INTRODUCTION

Unhealthy dietary habits are closely related to multiple chronic health problems such as overweight, diabetes, malnutrition, eating disorder, and cardiovascular diseases [1].

Chunzhuo Wang, T. Sunil Kumar, and Bart Vanrumste are with the e-Media Research Lab, and also with the ESAT-STADIUS Division, KU Leuven, 3000 Leuven, Belgium (e-mail: chunzhuo.wang@kuleuven.be; sunilkumar.telagamsetti@kuleuven.be; bart.vanrumste@kuleuven.be).

Walter De Raedt and Chunzhuo Wang are with the Life Science Department, IMEC, 3001 Heverlee, Belgium (e-mail: Walter.DeRaedt@imec.be).

Guido Camps is with the Division of Human Nutrition and Health, Department of Agrotechnology and Food Sciences, Wageningen University and Research, 6700EA Wageningen, and also with the OnePlanet Research Center, 6708WE Wageningen, The Netherlands (e-mail: guido.camps@wur.nl).

Hans Hallez is with the M-Group, DistriNet, Department of Computer Science, KU Leuven, 8200 Sint-Michiels, Belgium (e-mail: hans.hallez@kuleuven.be).

These dietary related diseases can not only affect individual's daily life but also result in substantial financial and societal costs [2]. According to WHO reports, the overweight and obesity has been considered as a global public health problem affecting people's quality of life (QoF) [3] and imbalanced diet is the primary cause of this issue. In order to keep a healthy diet, it is necessary to track the dietary intake.

Recently, different automatic food intake monitoring systems have been proposed for this purpose. These solutions can be categorized into 3 types: video-based, wearable sensor-based, and portable sensor based approaches. The video-based method [4]–[6] uses cameras and processes video signals to detect eating gestures. The wearable sensor-based approach mainly utilizes an inertial sensor [7], a miniature camera [8] or an acoustic sensor [9] to monitor hand-to-mouth movements or chewing movements. The smart plate [10], the dining tray [11], and the smart table surface [12] are categorized into the portable sensor based approach.

The existing methods have been proved to be feasible for food intake monitoring; however, some disadvantages can emerge: The wearable sensors require precise placement, which can be uncomfortable to wear for long-term duration. The battery concern is also associated with such types of sensors. As for a video-based food intake monitoring system, lighting conditions and privacy issues may be concerned. In order to account for these drawbacks, we propose a contact-less, privacy-preserving radar-based approach for in-home food intake monitoring.

Recently, radar, as an emerging technology, combined with machine learning, has been gradually applied to a variety of scenarios, such as automotive driving, health monitoring (e.g., vital sign monitoring [13], fall detection [14]), and human activity recognition (HAR).

Much radar-based HAR research in indoor/kitchen scenarios has been conducted [15]–[17]. Luo et al. [15] used the Doppler-Time map (DT map) from two radars and a convolutional neural network (CNN) to recognize 15 activities (eating activity included) from 3 participants in a kitchen environment, and they achieved an overall classification rate of 92.8%. Gorij et al. [16] deployed two radars (one on the wall, one on the ceiling) to classify 8 activities of 12 participants, and with this approach they obtained a weighted F1-score of 93.63% (88.26% for eating activity detection). They

manually extracted features and used a Random Forest (RF) classifier. Maitre et al. [17] utilized Range-time maps (RT map) from three ultra-wideband (UWB) radars and applied a CNN and long-short-term-memory network combined model (CNN-LSTM) to recognize 15 different activities from 10 participants. They yielded an F1-score of 90% (93% for eating activity detection). It should be noted that the above research mainly focuses on multi-activities recognition. For each activity, they can classify the session/period coarsely. Specifically, they recognized the eating session from the start to the end, but did not recognize fine-grained eating gestures.

The fine-grained eating gesture recognition includes details such as how many eating gestures happened in that period (counting the number of eating/drinking gestures) and the duration of each detected gesture. In this research, the eating gesture is defined as the movement from raising the left/right hand to the mouth with the fork/knife/spoon/chopsticks until putting away the hand from the mouth. The movement from raising the left/right hand to the mouth with a container until putting away the container from the mouth is considered as a drinking gesture.

Xie et al. [18] were the first to explore the potential of using mmWave Frequency Modulated Continuous Wave (FMCW) radar sensors for fine-grained eating behavior monitoring. They collected 1000 eating gestures with five classes (fork, fork & knife, spoon, chopstick, and bare hand) from 6 participants. They detected the eating gestures by searching the repetitive pattern of hand and arm movements that bring food to the table to mouth. They determined an eating gesture detection by setting the number of repeated movements to 5. Once an eating gesture was detected, they removed points with low velocity by an empirical threshold, then they used an unsupervised clustering method to segment each detected eating gesture. After segmentation, a CNN-based classifier was used to classify the segmented data. Their approach contains multiple empirical-determined parameters and is therefore not an automated monitoring system. In a recent work [19], the authors collected a total of 162 eating gestures and 162 drinking gestures from 6 participants in a standing scenario (not sitting in front of a dining table, which is a more common way of eating). By using CNN-BiLSTM model, they achieved 84% accuracy in detection of eating activity and 76% accuracy of drinking activity detection under Leave-One-Subject-Out (LOSO) validation scheme.

Apart from the aforementioned issues, the previous radar-based eating activity recognition works do not collect data in real meal sessions. In [15], the average duration for eating activity is 4.17 min. In [16], each participant's eating and drinking duration is 3.5 min. In [17], each participant has a 0.5 min drinking recording and a 2 min eating recording. However, the real meal session is a more realistic and challenging scenario with a longer duration (10-20 min per meal in our case, see Table 2). The eating activities in one meal session are continuous with different durations and different time gaps between two eating gestures [20]. In this paper, we build a new end-to-end approach for fine-grained eating and drinking gesture detection using a contactless mm-Wave FMCW radar and 3D temporal convolutional

network (3D-TCN). The key highlights of this work are as follows:

- 1) A novel radar-based system is applied to detect eating gestures during meal sessions. Using the FMCW radar system, we produce a publicly available dataset¹ with 48 meal sessions from 48 participants. In total, 3121 eating gestures and 608 drinking gestures are recorded. To our best knowledge, this is the first public radar dataset that focuses on eating gesture detection in real meal sessions. This is also the largest radar-based food intake dataset in the literature.
- 2) A novel sequence-to-sequence (seq2seq) 3D-TCN model is designed to process Range-Doppler Cube (RD Cube) for detecting in-meal food intake gestures and segmenting the time interval of the eating/drinking gesture. In addition to the food intake monitoring purpose, the obtained interval of eating gestures can be used to investigate the motion features of eating gestures, such as the time used for an eating gesture.
- 3) We benchmarked different design choices of the 3D-TCN with the state of the art techniques reported in literature. Firstly, different radar data representations, namely Range-Doppler Cube (RD Cube) and Doppler-Time map (DT map), are selected to find the most suitable one based on machine learning performance. Secondly, different models (CNN-LSTM, CNN-BiLSTM) are used to compare the performance.

The rest of this paper is organized as follows: Section II describes the theory of a FMCW radar and the detailed pipeline of the proposed approach. In section III, we present the design of different experiments. Section IV shows the results. The discussion part is in Section V. The conclusions of the whole work are made in Section VI.

2 METHODS

2.1 FMCW radar principle

For an FMCW radar with single transmitter (TX) and single receiver (RX), as called single-input-single-output (SISO) radar, its TX periodically transmits a frequency modulated sinusoidal signal with bandwidth B , start frequency f_c , frequency slope S , period T_c , as shown in Fig. 1. The signal in one periodic time is called a chirp signal. A sequence of chirps represents a frame (Fig. 1(c)(d)). The row dimension of the frame is called the fast time dimension, and the column dimension is known as the slow time dimension, as the time scale between two chirps is much larger than the time scale between two sample points within a chirp. The RX antenna receives the signals reflected from objects in the radar's field of view (FOV). By mixing the received signal and transmitted signal, the mixer generates the Intermediate Frequency (IF) signal, also called the beat signal. The instantaneous frequency (f_b) of IF signal is equal to the difference of the instantaneous frequency between the transmitted and received signal. Similarly, the phase of IF signal (ϕ) is the

1. <https://github.com/Pituohai/Eat-Radar>

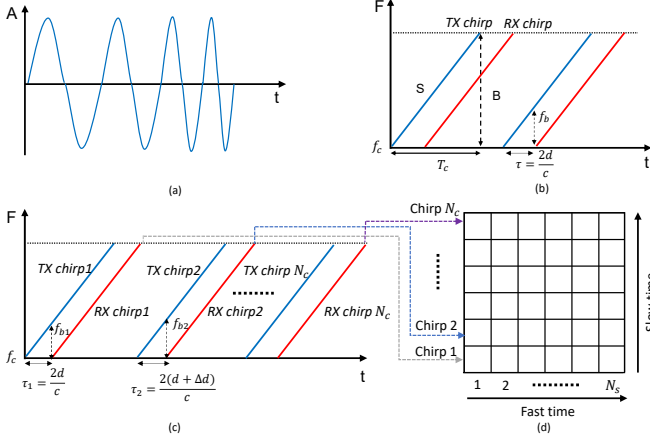


Fig. 1. (a) An example of the time-amplitude response from radar TX signal. The x-axis represents the time (t), and the y-axis represents the amplitude (A) of the signal. (b) The time-frequency response of TX signal (blue line) and RX signal (red line). The x-axis represents the time (t), and the y-axis represents the frequency (F). B , f_c , S , T_c are the bandwidth, start frequency, slope, and period of TX signal. f_b , d , c , τ are the beat frequency, the distance between the radar and the object, the speed of light, and the time delay between TX and RX signal. (c) The consecutive TX and RX signals for a moving object. τ_1 , τ_2 represent the time delay for the first and second chirp, Δd is the displacement of the moving target in one TX period. (d) The form of the initial data frame after mixing TX and RX signals. Each row represents the N_s sample points for a chirp after mixing and analog to digital conversion (ADC), N_c chirps are stacked together to form the initial data frame. The row dimension of the frame is called the fast time dimension, and the column dimension is known as the slow time dimension, as the time scale between two chirps is much larger than the time scale between two sample points in a chirp.

difference of phase between the transmitted and received signal.

2.1.1 Range measurement

As shown in Fig. 1 (b), for a static object with a distance d to the radar, the time delay of the received signal is calculated as $\tau = \frac{f_b}{S} = \frac{2d}{c}$, where c is the speed of light. Hence, the relation between the range d and beat frequency f_b is $d = \frac{f_b c}{2S}$. To calculate the range, a Fast Fourier Transform (Range-FFT) is applied to convert the IF signal from the time domain to the frequency domain for each chirp. The initial phase (ϕ) of the IF signal is indicated as $\phi = 2\pi f_c \tau = \frac{4\pi d}{\lambda}$, where λ is the wavelength.

2.1.2 Velocity measurement

For a moving object with range d and velocity v , there is a tiny displacement Δd between two consecutive chirps, as shown Fig. 1 (c). This causes an IF frequency change $\Delta f_b = f_{b2} - f_{b1} = S(\tau_2 - \tau_1) = S(\frac{2(d+\Delta d)}{c} - \frac{2d}{c}) = \frac{2S\Delta d}{c}$ and a phase change $\Delta\phi = \frac{4\pi\Delta d}{\lambda} = \frac{4\pi v T_c}{\lambda}$. Normally, the Δf_b caused by Δd is negligible compared to the scale of the sweep bandwidth (B), whereas the phase change is more sensitive to the object's movement between chirps in one frame. Hence, to estimate the velocity, an FFT across the chirps (along slow time axis, see Fig. 1(d)) for each range bin in one frame is applied after Range-FFT processing, as called Doppler-FFT. More details of the FMCW radar principle are introduced by the website of Texas Instruments (TI)².

2. See <https://training.ti.com/node/1139153>

TABLE 1
Configurations of FMCW radar

Parameter	Configuration
Start Frequency	77 GHz
Sweep Bandwidth	3.8 GHz
Sweep slope	50 MHz
Frame rate	25 fps
Sampling frequency	2000 ksp/s
Number of chirps in one frame	128
Number of samples in one chirp	128
Number of used transmitter, receivers	1, 4
Range resolution	4 cm
Velocity resolution	4 cm/s

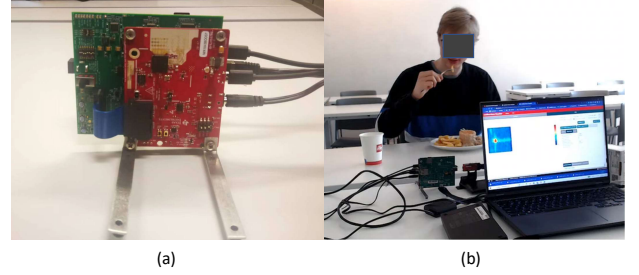


Fig. 2. (a) The TI IWR1843 radar board (Red) and DCA1000EVM board (Green). (b) The scene of data collection. Participants are eating with a pair of fork & knife. The radar is placed on the table in front of the participant.

It should be noted that an analog to digital conversion (ADC) is used to digitize the beat signal before any processing (e.g., Range-FFT, Doppler-FFT). Suppose the number of samples in a chirp is N_s after the ADC and the number of chirps in a frame is N_c , the dimension of a radar data frame R is $N_c \times N_s$ (Fig. 1 (d)).

2.2 Radar system information

The experiment utilizes a 76GHz TI IWR1843 radar boost board and a DCA1000EVM data capture card to build the data collection system, as shown in Fig. 2. The configurations of the general radar system parameters are specified in Table 1. The radar board has a 4 GHz bandwidth, with 2 TX and 4RX antennas. The system is powered with 5 V. The configured radar system generates 25 frames per second (fps). Two USB interfaces (one for IWR1843 radar board, one for DCA1000EVM) are connected to the laptop for system configuration. One Ethernet cable with high-speed data transmission capability (1 Gbps) is used to transfer raw data from the radar to laptop via the software TI mmWave Studio³. The raw data are then processed via Matlab R2020b.

2.3 Radar signal processing

The raw data exported from the radar are defined as a 5D data cube of size $N_{fm} \times N_{tx} \times N_{rx} \times N_c \times N_s$ where N_{fm} , N_{tx} , N_{rx} , N_c and N_s are the numbers of the radar frames in one meal session, transmitters (1), receivers (4), chirps in one frame (128), and sample points (128) in one chirp,

3. See <https://www.ti.com/tool/MMWAVE-STUDIO>

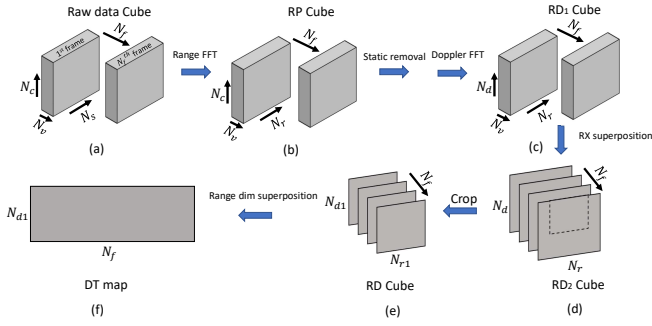


Fig. 3. The radar signal pre-processing pipeline. (a) The raw data cube. N_f represents the number of radar frames in one meal, N_c represents the number of chirps in one frame, N_s is the number of sample points in one chirp, N_v denotes the number of virtual antennas. (b) The range profile cube (RP Cube). N_r is the number of range bins in one chirp after range-FFT. (c) The RD_1 Cube. N_d represents the number of doppler bins in one frame after doppler-FFT. (d) The RD_2 Cube after RX superposition. (e) The cropped RD Cube (to reduce the computation cost). The N_{r1} and N_{d1} represent the range size and doppler size of cropped frames in RD Cube. (f) The Doppler-time map (DT map).

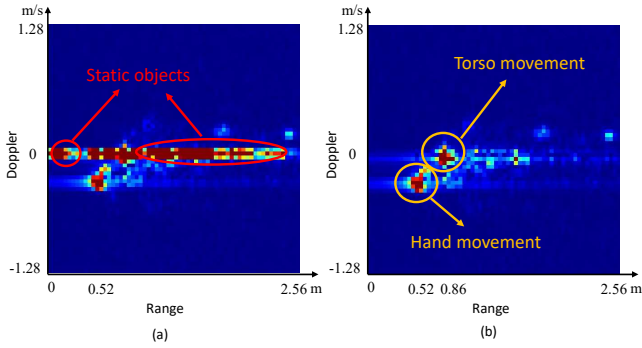


Fig. 4. The range-doppler (RD) frame represents the transient movement taking a glass of water from table to mouth. (a) the RD frame without static object removal; (b) the RD frame after static object removal. This is a movement from plate to mouth (the hand is moving away from radar), so it has negative velocity. The torso (body) is moving towards the radar with lower velocity compared to the hand. It should be noted that the size of the RD in this figure is 64×64 for the visualization convenience, whereas the actual size of cropped RD frame is 64×32 .

respectively. Considering that we only use 1 transmitter and 4 receivers, the term $N_{tx} \times N_{rx}$ is replaced with N_v which denotes the number of virtual antennas ($N_v = 4$). Hence, a 4D data cube $N_{fm} \times N_v \times N_c \times N_s$ represents the raw data of a meal session. As mentioned in Section II-A, a frame of a SISO radar is represented by R (with size $N_c \times N_s$, Fig. 1 (d)), the 4D data cube can also be written in $N_{fm} \times N_v \times R$. Subsequently, several steps are applied to extract the meaningful features, as shown in Fig. 3.

2.3.1 Range FFT

For each frame R , we apply a FFT transform along fast-time axis (in each chirp, see Fig. 1 (d)), obtained range profile cube (RP Cube) with size $N_{fm} \times N_v \times N_c \times N_r = N_{fm} \times N_v \times R_1$, N_r represents the number of range bins after range-FFT, R_1 represents the new frame in range profile cube (RP Cube). In this research $N_r = N_s = 128$, so the frame size is the same.

2.3.2 Static objects removal

The data were collected in different locations with different stationary layouts. To remove the signal of static objects, for each frame R_1 in the RP Cube, we calculate the average value through all chirps (along the slow-time axis, see Fig. 1 (d)), and every original chirp is subtracted by the mean chirp as follows [21]:

$$R_2(i, j) = R_1(i, j) - \frac{1}{N_c} \sum_{k=1}^{N_c} R_1(k, j) \quad (1)$$

where $R_1(i, j)$ represents the value at i -th chirp ($i \in [1, N_c]$) and j -th range bin ($j \in [1, N_r]$) in frame R_1 , R_2 represents the new frame after removing static objects.

2.3.3 Doppler FFT

For each frame R_2 , we apply a FFT along slow-time across chirps to generate a Range-Doppler cube (RD_1 Cube) with size $N_{fm} \times N_v \times N_d \times N_r = N_{fm} \times N_v \times R_3$, N_d represents the number of doppler bins after doppler-FFT, R_3 represents the new frame in RD_1 Cube. In this research $N_d = N_c = 128$, so the frame size is the same.

2.3.4 RX superposition

Because of the narrow width (less than 1m) of the moving target (human), the angular resolution obtained by 4 receiving antennas is insufficient to differentiate objects in the cross-range dimension. Therefore we simply superpose the RD_1 Cubes from 4 RX channels into one with an improved signal-to-noise ratio (SNR) [22]. The new RD_2 Cube has size $N_{fm} \times N_d \times N_r = N_{fm} \times R_4$, R_4 represents the new 4-in-1 RD frame:

$$RD_2(t, i, j) = \frac{1}{N_v} \sum_{a=1}^{N_v} |RD_1(t, a, i, j)| \quad (2)$$

where $RD_2(t, i, j)$ represents the value at t -th frame ($t \in [1, N_{fm}]$) i -th doppler bin ($i \in [1, N_d]$) and j -th range bin ($j \in [1, N_r]$), a represents the order of the virtual antennas ($a \in [1, N_v]$).

2.3.5 Crop ROI

The obtained RD_2 Cube contains frames with size 128×128 . Because this research is focused on short-range activity recognition, and food intake behavior has low speed, it is observed that the long-range area and high-velocity area are never reached in the RD frames. To reduce the computation cost, we crop the frames from RD_2 Cube to keep the region of interest (ROI) and remove the redundant area. The cropped frame size is $N_{d1} \times N_{r1}$, where $N_{d1} = 64$ (max velocity: $\pm 1.28m/s$) and $N_{r1} = 32$ (max range: $1.28m$). After this step, the final RD Cube is prepared as 3D input data with size $N_{fm} \times N_{d1} \times N_{r1}$ ($N_{fm} \times 64 \times 32$). It should be noted that the initial frame size of the radar data is associated with the range resolution and doppler resolution, so we tend to generate a large initial frame size to obtain a fine resolution and crop the ROI afterwards. Fig. 4 shows the example of an RD frame.

2.3.6 Generate the Doppler-Time map for comparison

This extra step is used to generate the Doppler-Time map (DT map) for further data representation comparison, which will be discussed in Section III-C. The DT map is generated by summing the absolute value of the signal over the range dimension [23].

$$DT(t, n) = \frac{1}{N_{r1}} \sum_{j=1}^{N_{r1}} RD(t, n, j) \quad (3)$$

where $DT(t, n)$ represents the DT map value at t -th frame ($t \in [1, N_{fm}]$) and n -th doppler bin ($n \in [1, N_{d1}]$), $RD(t, n, j)$ represents the RD Cube value at t -th frame, n -th doppler bin, and j -th range bin ($j \in [1, N_{r1}]$). The dimension of the DT map is $N_{fm} \times N_{d1}$.

2.4 Data collection and annotation

The ethical committee of KU Leuven has approved this research (Reference number: G-2021-4025-R4), and written informed consent from each participant was collected during data collection. 48 participants (16 females and 32 males) were recruited to take part in the experiment. Each of them had one meal session. The data were collected in seven different rooms with different layouts at the KU Leuven University Campus GroupT (One Staff Office, Three Classrooms, Two Meeting rooms, One Study room). The total duration of the collected dataset is 783 min. The average duration of each meal is 16.32 ± 4.74 min. The participants sat directly in front of the radar and ate their meal. The distance between the food plate and the radar was around 0.3 m to 0.6 m, as shown in Fig. 2 (b). A camera was used to record video for annotation. It should be noted that some of the participants also wore IMU wristbands on two hands for another study, which will not be discussed here. Table 2 shows the detailed information of meals. The dataset used in this paper is available at <https://github.com/Pituohai/Eat-Radar>.

2.4.1 Eating activity setting

The consumed food contains salad, fries, chicken, fried noodles, rice, sandwiches, and cakes, served by Alma (the student restaurant of KU Leuven), a Chinese restaurant, a sandwich shop, and a convenience store. The participants could use forks & knives, chopsticks, spoons, and hands to eat the meal. For participants who ate with their hands, they could use one hand or two hands to eat food. The participant was allowed to eat at their own pace. They could stop, talk, watch smartphones, move for a while, and prepare/stir food. It should be noted that each participant could only use one eating style in one meal session. Detailed information on eating styles is shown in Table 3.

2.4.2 Drinking activity setting

The drinking activity is also considered in this experiment. A glass of water or a can of soft drink selected by the participant was served together with the meal. Participants can drink with either hand, or both hands. During the meal, the participants could drink at their own pace. However, to increase the number of drinking gestures, some participants were required to drink several times extra before and after

TABLE 2
Meal data statistics

Parameter	Values
Participants	48
Fork & knife: chopsticks:spoon:hand	19:15:5:9
Male : Female	32 : 16
Duration ratio of other : eating : drinking	11.09:2.71:1
Mean meal duration	(16.32±4.74) min
Total duration	783 min

TABLE 3
Details of different eating styles

Style	#Eating gesture	Food
Fork & Knife	1232	salad, fries, chicken, beef burger, cake
Chopsticks	1349	rice, fried noodles, chicken, vegetables
Spoon	256	rice, chicken, vegetables
Hand	284	chicken sandwich, egg sandwich

the meal. This requirement is due to the fact that people have few drinking gestures compared to the amount of eating gestures and other gestures in a meal.

We used ELAN [24] to annotate the video. The data are annotated into 3 classes, namely eating, drinking, and other. The definitions of eating and drinking gesture are mentioned in Section I. It should be noted that the food intake gestures are diverse among different participants; even for the same participant, the gestures can be different during one meal. Therefore, the defined end point of the annotated food intake gesture is putting the hand away from the mouth, not strictly putting the hand back to the plate or table. The annotation work was performed by two annotators who followed the same eating/drinking definition. One is the first author, the other one is independent of this research. The annotation work was divided by sequence. The first author reviewed the annotation from the independent annotator and adjusted it if needed to minimize ambiguity. There are 3121 eating gestures and 608 drinking gestures in total. The dataset statistics are indicated in Table 4. Fig. 5 shows the video frames and the corresponding RD frames of different eating and drinking gestures.

2.5 Sequence-to-Sequence Neural Network Architecture

Several deep learning models have been proposed to solve activity recognition tasks. Before feeding the data into the model, prior works [15]–[17] tend to use a sliding window to generate data segments with fixed temporal length. For each window, there is only one label made by majority voting. Alternatively, they label the window by checking if it contains an entire target activity. We found both approaches have limitations for real-world continuous eating gesture detection. The challenge lies in the various durations of eating gestures and the fixed length of the sliding window. Firstly, if the duration of the eating gesture is longer than the window length, this gesture will be divided into two segments or even more. The segment that contains the minor part of the eating gesture may be labeled as other.

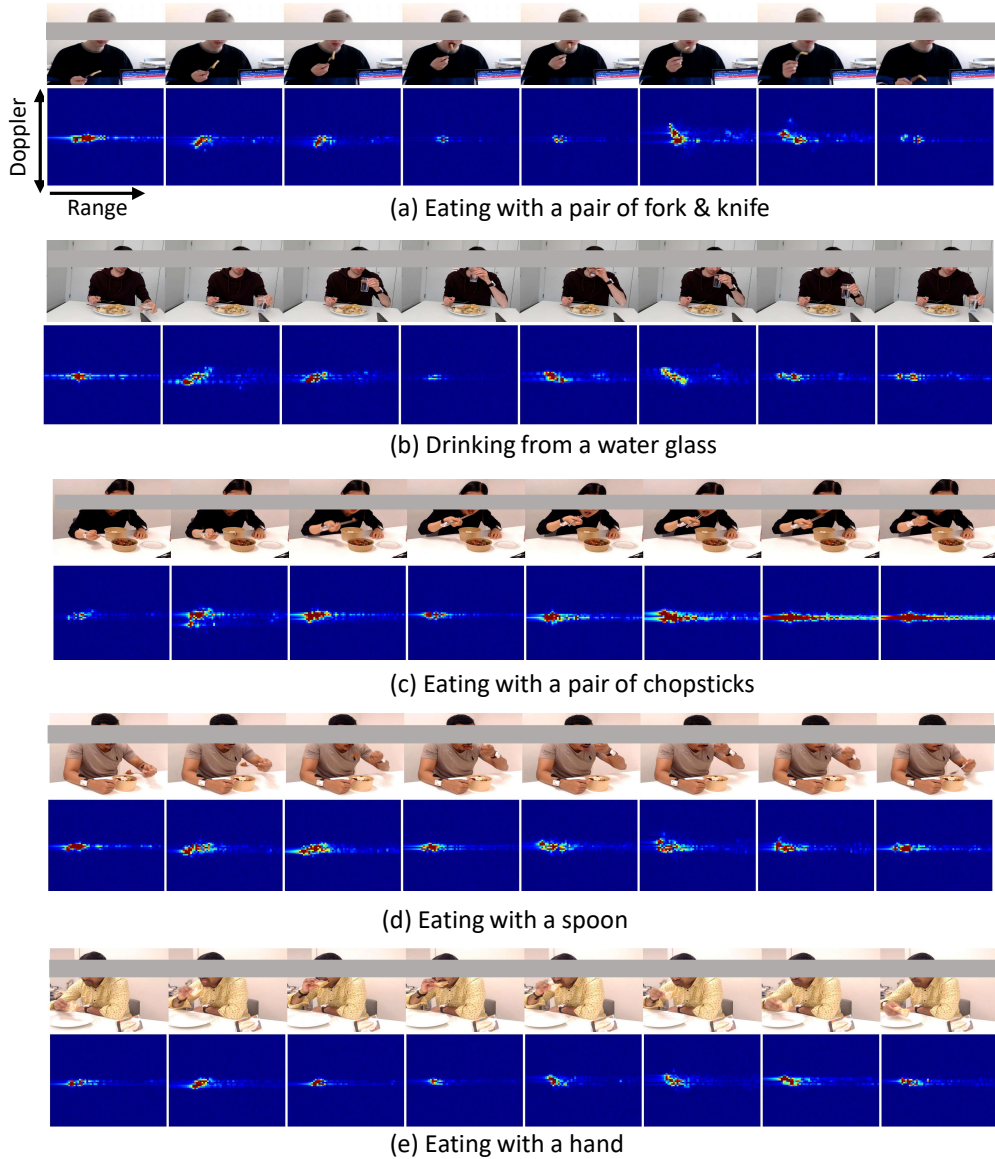


Fig. 5. The video frames and the corresponding RD frames of different eating and drinking gestures. For the RD frames, the x-axis represents the range dimension; the y-axis represents the doppler dimension. It should be noted that the actual amounts of frames for each eating/drinking gesture are different, and we manually selected the fixed number of frames for each gesture in this figure.

TABLE 4
Eating and Drinking gesture Details

Parameter	Values	
	Eating	Drinking
Number of gestures	3121	608
Duration range of gestures	1.04-17.08 s	2.36-20.60 s
Median duration of gestures	2.40 s	4.68 s
Mean \pm Std of gestures	2.76 ± 1.32 s	5.22 ± 2.14 s

Secondly, if one window contains several eating gestures with a short duration, it is not able to count the number of eating gestures.

To address this issue, we choose the seq2seq architecture instead of the conventional many-to-one sliding window

based architecture. For the seq2seq model, the prediction is generated for each data point/frame rather than a window, and this is called frame-wise prediction. Afterward, a sequence of frame-wise predictions with the same value is considered as a segmental interval.

The temporal convolutional network (TCN) that using dilated convolution and skip connection is first proposed by Lea et al. [25] to recognize long-range temporal sequences. To date, it has been utilized to process time-series signals in the healthcare and disease diagnosis domains [26]–[28]. Its outstanding ability in time-series signal processing is demonstrated in [29]. The existing TCN architectures [25], [30] are not suitable for the radar-based eating activity detection, as we employ 3D data in our experiments. Therefore, in this research, we developed the 3D-TCN using Conv3D to process time-series RD Cube.

As illustrated in Fig. 6 (a), the skeleton of the 3D-TCN

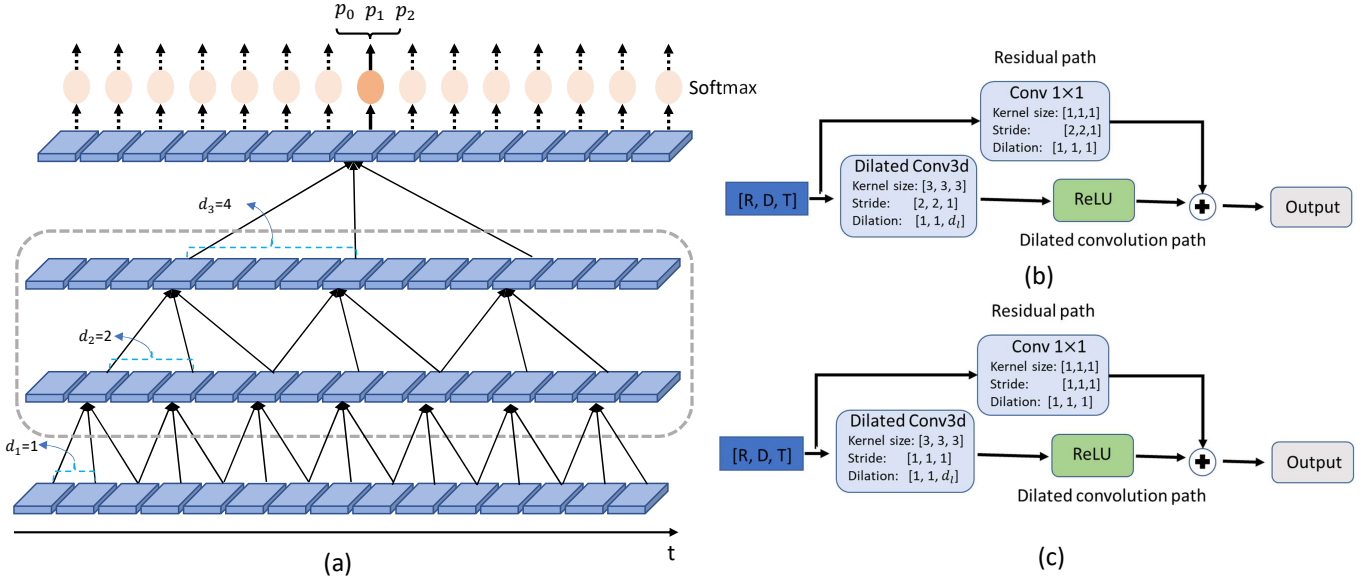


Fig. 6. (a) The framework of the 3D-TCN model. From bottom to top, the RD cube is sent into the input layer (the first layer). The dilation factor of the first layer d_1 is 1, and the dilation factor of subsequent layers doubled from bottom to top ($d_2 = 2, d_3 = 4$) to increase the receptive field. After the last dilated residual layer, a softmax activation is applied to generate prediction according to the feature extracted from previous layers. It should be noted that the output of 3D-TCN is frame-wise; we only explicitly indicate the 3 class prediction (p_0, p_1, p_2) for one frame in this example. (b) The detailed architecture of the shape-variant dilated residual layer. (c) The detailed architecture of the shape-invariant dilated residual layer. The main difference between the two layers is the stride setting. d_l represents the dilated factor, $d_l = 2^{l-1}$ ($1 \leq l \leq L$), where l denotes the order of layers. The $[R, D, T]$ in the input block of (b) and (c) represent the range dimension (R), doppler dimension (D), and time dimension (T) of input data.

TABLE 5

The architecture of 3D-TCN model and the output size of each layer.

Layer	Type ^a	Output
Input ^b	-	$1 \times 32 \times 64 \times 1000$
Layer 1	Shape variant ^c	$32 \times 32 \times 32 \times 1000$
Layer 2	Shape variant	$32 \times 16 \times 16 \times 1000$
Layer 3	Shape variant	$32 \times 8 \times 8 \times 1000$
Layer 4	Shape variant	$32 \times 4 \times 4 \times 1000$
Layer 5	Shape invariant	$32 \times 4 \times 4 \times 1000$
Layer 6	Shape invariant	$32 \times 4 \times 4 \times 1000$
Layer 7	Shape invariant	$32 \times 4 \times 4 \times 1000$
Layer 8	Shape invariant	$32 \times 4 \times 4 \times 1000$
Layer 9	Shape invariant	$32 \times 4 \times 4 \times 1000$
Flatten	-	512×1000
Conv1D	-	3×1000
Softmax	-	3×1000

^a There are two types of dilated residual layer, namely the shape variant layer and the shape invariant layer, as shown in Fig. 6 (b) and Fig. 6 (c).

^b Here we take a 40s data segment for example. The data frequency is 25Hz (25 frames per second) and each frame has the size of 64×32 (Doppler \times Range), hence the input data size is $1 \times 32 \times 64 \times 1000$ (num_channels \times range_dim \times doppler_dim \times num_frames).

^c The first shape variant layer is different from others; its stride is $[1, 2, 1]$, the size of range dimension remains the same to achieve the same size between range and doppler dimension.

model contains a series of L dilated residual layers, where L is the number of layers. Each layer consists of dilated convolutions with RELU activation, and a residual connection that combines the input of the current layer and the convolution results together, as depicted in Fig. 6 (b). The Conv3D kernel with size $3 \times 3 \times 3$ convolves input data in range (R), doppler (D), and time (T) dimensions. The number of Conv3D kernels in each layer is 32. The 3D-TCN contains

2 types of dilated residual layers, the shape-invariant layer and the shape-variant layer. The shape-variant layer (Fig. 6 (b)) is used to reduce the number of parameters. Specifically, the size of the range and doppler dimensions are reduced whereas the time dimension remains by setting the stride as $(2, 2, 1)$ for the shape-variant layer. The residual connection has the same stride to keep the same reduction. In contrast, the input and output dimensions of shape-invariant layer (Fig. 6 (c)) remain the same by setting the stride as $(1, 1, 1)$. The convolutions in both layers are in SAME mode. Finally, the dilation only applies in the time dimension; for the range and doppler dimension, the dilation rate is 1. The dilation factor of the time dimension in Conv3D at each layer is doubled such that $d_l = 2^{l-1}$ ($1 \leq l \leq L$). The 3D-TCN in Fig. 6 is a non-causal type, meaning that the outcome depends not solely on past data, but also on future data. Following the last dilated residual layer, a softmax activation is applied to generate a prediction based on the feature retrieved from preceding layers. The formula for calculating the length of the receptive field for non-causal 3D-TCN is $r(L) = 2^{L+1} - 1$, where L denotes the depth of the network (number of layers).

The loss function of the 3D-TCN model is a combination of the classification loss and the smoothing loss. Firstly, a cross-entropy loss is applied as the classification loss:

$$\mathcal{L}_{cls} = \frac{1}{T} \sum_{t,c} -y_{t,c} \log(\hat{y}_{t,c}) \quad (4)$$

where $y_{t,c}$ represents the ground truth label, $\hat{y}_{t,c}$ is the predicted output for class c at time t .

Secondly, a truncated mean squared error (MSE) over sample-wise log-probabilities [26] is used as the smoothing

loss:

$$\mathcal{L}_{T-MSE} = \frac{1}{TC} \sum_{t,c} \tilde{\Delta}_{t,c}^2 \quad (5)$$

$$\tilde{\Delta}_{t,c} = \begin{cases} \Delta_{t,c} : \Delta_{t,c} \leq \gamma \\ \gamma : otherwise \end{cases} \quad (6)$$

$$\Delta_{t,c} = |\log(\hat{y}_{t,c}) - \log(\hat{y}_{t-1,c})| \quad (7)$$

where T is the temporal length of data, C is the number of classes, and $\hat{y}_{t,c}$ is the probability of class c at time t .

The complete loss function \mathcal{L} is obtained by combining the two types of loss :

$$\mathcal{L} = \mathcal{L}_{cls} + \lambda \mathcal{L}_{T-MSE} \quad (8)$$

where λ is a parameter to determine the weights of the two losses. We select $\gamma = 4$ and $\lambda = 0.15$ for the loss function according to [26].

The code of the 3D-TCN is modified from [26]. After each dilated layer, a 30% dropout is applied. According to experiments, we build the 3D-TCN with 9 layers, 4 for shape variant layers, and 5 for shape invariant layers, so the receptive field is 1023 frames. To train the model, an Adam optimizer with a learning rate of 0.0005 is employed. It should be noted that there is a temporal lag for prediction due to its non-causal characteristic. The temporal delay is calculated as dividing half of the receptive field by the sampling frequency ($0.5 \times 1023 / 25 = 20s$). The architecture information is summarized in Table 5.

All the training, validation, and testing experiments are deployed on an Intel 8-core Xeon Gold 6240 CPUs@2.6 GHz (Cascadelake) with 20 GB RAM per core, and two pieces of NVIDIA Tesla V100-SXM2-32GB GPU from Vlaams Supercomputer Centrum (VSC)⁴.

3 EVALUATION AND EXPERIMENTS

3.1 Evaluation scheme

3.1.1 Frame-wise evaluation

To evaluate the performance of a seq2seq model, firstly, a frame-wise confusion matrix, the most commonly used evaluation index is employed. Secondly, as our dataset is unbalanced (See Table 2), and the goal of this research is multi-class classification, f1-scores for eating and drinking frames are calculated. Finally, the Cohen Kappa is applied as an overall frame-wise metric. The mathematical equations involved in the computations of aforementioned evaluation metrics are given below.

$$f1-score_{c=\{E,D\}} = \frac{2tp_c}{2tp_c + fp_c + fn_c} \quad (9)$$

$$Kappa = \frac{P_o - P_e}{1 - P_e} \quad (10)$$

$$P_o = \sum_{c=N,E,D} \frac{tp_c}{Total} \quad (11)$$

$$P_e = \sum_{c=N,E,D} \frac{tp_c + fp_c}{Total} \times \frac{tp_c + fn_c}{Total} \quad (12)$$

Where $Total$ is the total number of data frames, c represents the class, N, E, D represent the class of other, eating gesture, and drinking gesture, respectively. The tp , fp , and fn are frame-wise true positive, false positive, and false negative, respectively.

However, in the perspective of activity detection and segmentation, frame-wise evaluation is unable to give us the results such as how many eating/drinking gestures are detected and segmented. To address this issue, we also utilized segment-wise evaluation.

3.1.2 Segment-wise evaluation

The segmental F1-score proposed by [26], [27] is applied to assess the segment-wise performance. Prior to calculating the segmental F1-score, the intersection over union (IoU) of each predicted food intake gesture is first computed. The IoU is defined as $\frac{A \cap B}{A \cup B}$, the ratio of overlap between temporal intervals of the ground truth segment (A) and the predicted segment (B). Fig. 7 shows the example of IoU calculation. Once the IoU of each food intake gesture is calculated, a selected threshold k is applied to determine segment-wise True Positive (TP), False Negative (FN) and False Positive (FP). Fig. 8 depicts the definition of TP, FN, and FP and show some examples. If the IoU of a segment pair is greater than the threshold k , it is a TP (Fig. 8 S2), otherwise it is an FN segment (Fig. 8 S1) or FP segment (Fig. 8 S3). The decision tree is as follows:

$$Segment = \begin{cases} TP, & IoU \geq k \\ FP, & IoU < k, length_{gt} < length_p \\ FN, & IoU < k, length_{gt} > length_p \end{cases} \quad (13)$$

Where $length_{gt}$ and $length_p$ are the time lengths of the ground truth eating/drinking gesture and predicted eating/drinking gesture, respectively. Additionally, if multiple predicted segments exist inside the range of a given ground truth eating/drinking gesture, only one is classified as a TP, all others are FP (Fig. 8 S4). Conversely, if a predicted segment spans multiple ground truth eating/drinking gestures, only one is recognized as TP and the remainder are considered as FN (Fig. 8 S5). We also defined the corresponding punishment for the misclassification between the eating and drinking gesture (see Fig. 8 S8-S9). After the generation of segmental TP, FP, and FN, the segmental F1-score is calculated as:

$$F1-score_{c=\{E,D\}} = \frac{2TP_c}{2TP_c + FP_c + FN_c} \quad (14)$$

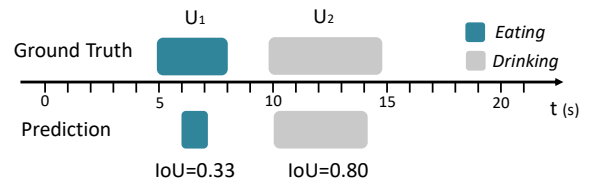


Fig. 7. The IoU example. For example U_1 , the ground truth eating gesture starts at 5s and ends at 8s (3s duration), the corresponding predicted eating gesture starts at 6s and ends at 7s (1s duration), hence the IoU is 0.33. Similarly, for example U_2 , the IoU is 0.80.

4. See <https://www.vscenrum.be/>

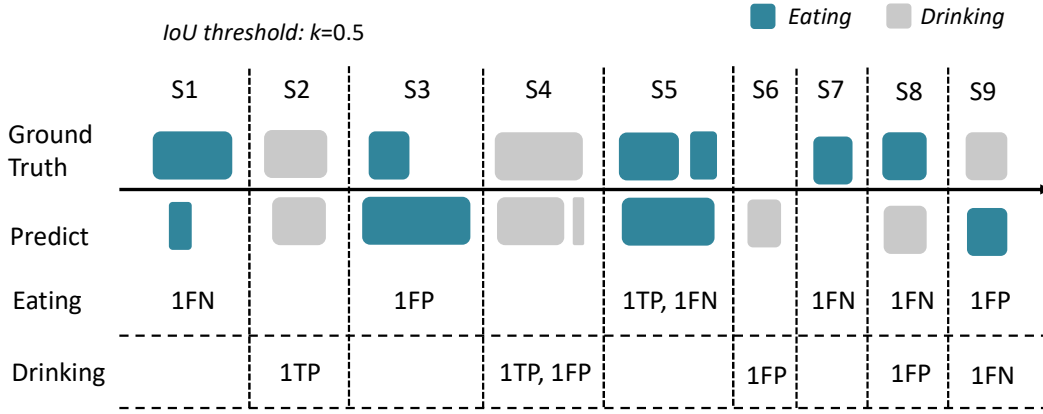


Fig. 8. Examples of the segment-wise evaluation. The threshold k is 0.5, if the computed IoU is less than 0.5, determine whether the segment belongs to FN or FP by comparing the length of the ground truth and prediction, S1 is FN and S3 is FP. The IoU of S2 is greater than 0.5, so it is a TP. If one ground truth segment covers two predicted segments, only one is counted, therefore S4 has 1 TP and 1 FP. Likewise, S5 contains 1 TP and 1 FN. If there is a predicted segment without a ground truth segment or a ground truth segment without a predicted segment, then there is 1 FP (S6) or 1 FN (S7). The examples S8 and S9 show misclassification cases between eating and drinking gestures.

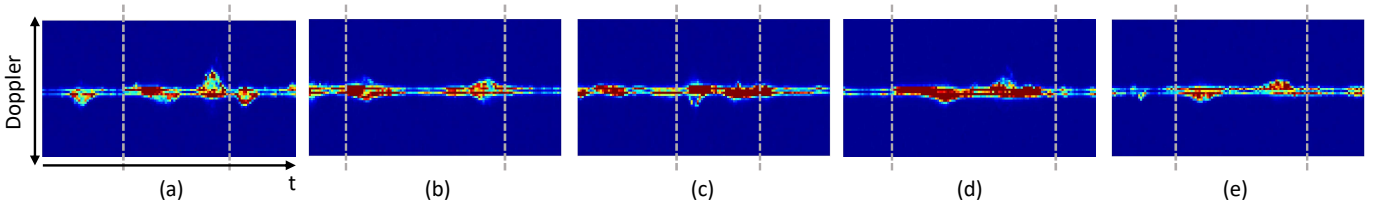


Fig. 9. Examples of DT map for different eating and drinking gestures shown in Fig. 5. The duration of each example is 5s. Signals between grey dashed line represent the eating and drinking gestures presented in Fig. 5. (a) Eating with a pair of fork&knife; (b) Drinking from a water glass; (c) Eating with a pair of chopsticks; (d) Eating with a spoon; (e) Eating with a hand.

Where c represents the class, E represents the eating class, D represents the drinking class. We calculated F1-scores for each class (eating and drinking).

The advantages of the segment-wise evaluation scheme are three-fold. Firstly, it penalizes over-segmentation errors (Fig. 8 S3) and under-segmentation errors (Fig. 8 S1); secondly, it allows minor temporal shifts between ground truth and prediction, which may be caused by annotation variability. Thirdly, it provides clear information including how many food gestures are detected and segmented. Three thresholds k are selected as 0.1, 0.25 and 0.5 according to [26], [27]. It should be noted that we use lower-case tp, fp, fn, and f1-score to represent frame-wise indices, and upper-case TP, FP, FN, and F1-score to denote segment-wise indices.

3.2 Models for benchmark

To compare the performance of the proposed approach, two different deep learning models are selected as benchmarks. Specifically, the normal CNN-LSTM model [31], and the CNN-Bidirectional LSTM (CNN-BiLSTM) model [32]. Both models can learn temporal context from time-series input data and have shown their capability in radar-based and video-based activity recognition. The basic skeletons of these models are inspired from [31], [32]; however, the hyperparameters (number of layers in CNN part, number of kernels in CNN part, number of hidden units in LSTM part, length of sliding window) are tuned to fit our dataset

(3D data). It should be noted that the output modes of LSTM and BiLSTM part are configured as sequence output.

3.2.1 CNN-LSTM

The CNN-LSTM model consists of three subnetworks: three CNN layers, one LSTM layer, and two fully connected layers (FCN). The CNN part is used to extract features from the RD frames, and the purpose of the LSTM part is to process the temporal information. The FCN uses the information from previous parts to classify the food intake behavior. The CNN part contains three layers with 16, 32, and 32 kernels with size 3×3 , respectively. The activation RELU is used for each layer. Each CNN layer is followed by a maxpooling layer with 2×2 pooling size. The output of the CNN part is flattened and fed into the LSTM part. The LSTM layer contains 128 hidden units followed by a 0.3 dropout. The FCN contains two dense layers. The first layer has 128 neurons with RELU activation, and the second layer has 3 neurons with Softmax activation. The Timedistributed layer is used to wrap the model.

3.2.2 CNN-BiLSTM

Compared to the normal CNN-LSTM network, the CNN-BiLSTM network utilizes a bidirectional LSTM layer (128 hidden units) instead of a unidirectional LSTM layer. The output of the bidirectional layer not only depends on previous RD frames but also takes future frames into considera-

TABLE 6
Overall frame-wise results for 8-fold cross-validation

Data	Model	Class	f1-score	Kappa
DT map (2D)	CNN-LSTM	E	0.506	0.423
		D	0.473	
	CNN-BiLSTM	E	0.526	0.471
		D	0.588	
	2D-TCN	E	0.718	0.675
		D	0.770	
RD Cube (3D)	CNN-LSTM	E	0.629	0.553
		D	0.625	
	CNN-BiLSTM	E	0.711	0.660
		D	0.735	
	3D-TCN	E	0.755	0.712
		D	0.784	

tion. The CNN part and FCN part are same as those of the normal CNN-LSTM model.

Different window lengths were explored to find the best performance of CNN-LSTM and CNN-BiLSTM. Based on experiments, the window length of CNN-LSTM and CNN-BiLSTM is 10 s and 20 s, respectively.

3.3 Radar data representations

For radar-based HAR systems, another common radar data representation is the DT map. Compared to RD Cube that contains range, velocity, and time dimensions, the DT map only includes information from time and velocity dimensions. For the eating activity, apart from velocity, the range information of the arm and the head (or torso) is also an essential feature. Thus, this research focuses on using RD Cube for eating gesture detection. To validate our hypothesis, we also test the DT map as input. For the 3D RD Cube, the data dimension is $N_f \times N_{d1} \times N_{r1}$, whereas the data dimension is $N_f \times N_{d1}$ for DT map. Fig. 9 shows the examples of DT map for different eating and drinking gestures presented in Fig. 5 with RD frames.

Due to the dimension difference between the DT map (2D) and the RD Cube (3D), proposed models used for the RD Cube (3D-TCN, (Timedistributed-) CNN-LSTM, (Timedistributed-) CNN-BiLSTM) are modified as 2D-TCN, CNN-LSTM, and CNN-BiLSTM to fit the DT map.

3.4 Validation strategy

To evaluate the model performance on unseen data, the dataset is divided into 8 folds. For each fold, 6 of 48 meals are selected as the test set, 6 meals are selected as the validation data, 36 meals are used for training. Hence the whole dataset can be tested after 8-fold experiment. It should be noted that the split of dataset in this validation method is based on meal-level, there is no information overlap between the train set, validation set, and test set. The meal_id lists for 8-fold experiments are available along with the dataset.

4 RESULTS

Table 6 presents the frame-wise eating and drinking f1-scores and overall kappa value for DT map and RD Cube.

It can be observed that both the f1-scores and kappa scores from three models in RD Cube are higher than those of in DT map. Using DT map data, the 2D-TCN obtains the highest performance with an overall kappa of 0.675, an eating f1-score of 0.718, and a drinking f1-score of 0.770. However, RD Cube obtains higher performance with 3D-TCN (kappa: 0.712, eating f1-score: 0.755, drinking f1-score: 0.784).

Table 7 shows the overall segment-wise results. Three thresholds ($k = 0.1, 0.25, 0.5$) are applied in this experiment. In segment-wise evaluation, the RD Cube still obtains better performance on all three models. For $k = 0.1$, the 3D-TCN model yields the highest F1-score of 0.915 for eating and 0.875 for drinking, compared to the CNN-LSTM (E: 0.810; D: 0.775) and the CNN-BiLSTM (E: 0.878; D: 0.857). When the threshold is raised to 0.5, the performance of all models decreases. However, 3D-TCN still obtains the best results (E: 0.887; D: 0.844) with the least reduction (E: 2.8%, D: 3.1%), compared to CNN-LSTM (E: 0.810→0.742; D: 0.775→0.689), and CNN-BiLSTM (E: 0.878→0.837; D: 0.857→0.801).

In addition to segmental F1-scores, the number of parameters of each model is also indicated in Table 7. For DT map data, the amount of parameters in 2D-TCN is the least (0.115M), whereas CNN-BiLSTM has the most parameters (0.442M). For RD Cube data, the number of parameters for all three models increased because of the dimension expansion of input data (from 2D to 3D). The CNN-BiLSTM still has the largest model size (0.573M). The CNN-LSTM and 3D-TCN have similar number of parameters, with 0.294M and 0.300M, respectively.

Table 8 shows the average segmental F1-score ($k=0.5$) across 8-fold cross-validation experiment. To further compare the performance difference between 3D-TCN and other models, paired t-test is applied ($N=8$). For eating gesture detection, the 3D-TCN obtains the highest mean F1-score (0.882 ± 0.042 , $p < 0.05$). For drinking gesture detection, the 3D-TCN still yields the highest mean F1-score with statistical significance (0.836 ± 0.077 , $p < 0.05$) for all models except 2D-TCN (0.821 ± 0.104 , $p = 0.12$).

Table 9 presents the number of misclassifications between eating gestures and drinking gestures for each model. The 3D-TCN wrongly predicted 20 ground truth eating gestures (0.64% of total ground truth eating gestures) as

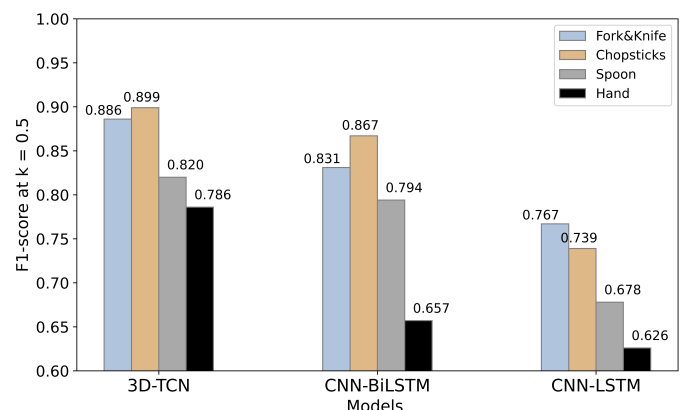


Fig. 10. The detection performance for four eating styles on three models. The y-axis represents the segmental F1-score for $k = 0.5$.

TABLE 7
Overall segmental results for 8-fold cross-validation

Data	Model	Class	$k = 0.1$				$k = 0.25$				$k = 0.5$				#Params
			TP	FP	FN	F1-score	TP	FP	FN	F1-score	TP	FP	FN	F1-score	
DT map (2D)	CNN-LSTM	E	1865	343	1255	0.700	1801	360	1302	0.684	1533	423	1524	0.612	0.228M ^a
		D	350	127	243	0.654	329	129	262	0.627	245	143	334	0.507	
	CNN-BiLSTM	E	1918	297	1202	0.719	1874	304	1239	0.708	1621	363	1440	0.643	0.442M
		D	433	132	160	0.748	415	135	175	0.728	345	144	239	0.643	
	2D-TCN	E	2740	391	381	0.877	2715	393	404	0.872	2547	441	526	0.840	0.115M
		D	548	117	60	0.861	538	120	67	0.852	505	125	98	0.819	
RD Cube (3D)	CNN-LSTM	E	2446	469	675	0.810	2414	481	695	0.804	2125	595	882	0.742	0.294M
		D	423	60	185	0.775	415	60	193	0.766	351	62	255	0.689	
	CNN-BiLSTM	E	2582	177	539	0.878	2557	183	558	0.873	2377	242	685	0.837	0.573M
		D	500	59	108	0.857	489	59	119	0.846	446	59	162	0.801	
	3D-TCN	E	2810	214	311	0.915	2796	222	317	0.912	2662	280	401	0.887	0.300M
		D	530	74	78	0.875	524	74	84	0.869	498	75	109	0.844	

^a The M represents million. So 0.228M represents 0.228 million parameters.

TABLE 8
Average results across 8-fold cross-validation for $k=0.5$

Data	Model	Class	F1-score (mean \pm std)	p^a
DT map (2D)	CNN-LSTM	E	0.606 \pm 0.081	***
		D	0.455 \pm 0.225	***
	CNN-BiLSTM	E	0.634 \pm 0.089	***
		D	0.630 \pm 0.126	***
	2D-TCN	E	0.835 \pm 0.055	**
		D	0.821 \pm 0.104	0.12
RD Cube (3D)	CNN-LSTM	E	0.739 \pm 0.049	***
		D	0.691 \pm 0.057	***
	CNN-BiLSTM	E	0.832 \pm 0.059	*
		D	0.811 \pm 0.065	**
	3D-TCN	E	0.882\pm0.042	-
		D	0.836\pm0.077	-

^a The p values are obtained by applying paired t-test (N=8 because of the 8-fold experiment) between 3D-TCN and other models for eating and drinking detection performance. $p < 0.05$: *, $p < 0.01$: **, $p < 0.001$: ***.

TABLE 9
Overall misclassification results. #(E \rightarrow D) denotes the number of ground truth eating gesture predicted as drinking gesture, refer to Fig. 8 S8. #(D \rightarrow E) represent the reverse case, refer to Fig. 8 S9.

Data	Model	#(E \rightarrow D)	#(D \rightarrow E)
DT map (2D)	CNN-LSTM	41(1.31%)	46(7.57%)
	CNN-BiLSTM	49(1.57%)	30(4.93%)
	2D-TCN	35(1.12%)	25(4.11%)
RD Cube (3D)	CNN-LSTM	39(1.25%)	37(6.09%)
	CNN-BiLSTM	22(0.70%)	30(4.93%)
	3D-TCN	20(0.64%)	29(4.77%)

drinking gestures (E \rightarrow D, see Fig.8 S8), which is the least. For the case of misclassifying drinking as eating (D \rightarrow E, see Fig.8 S9), 2D-TCN has the least number (25, 4.11% of total ground truth drinking gestures). For all models, the percentage of D \rightarrow E error is larger than that of E \rightarrow D error.

For eating gesture detection, four different eating styles are included in our dataset (Table 3). The detection perfor-

mance for each eating style on three models with RD Cube data is calculated, as shown in Fig. 10. The 3D-TCN obtains the highest F1-score for eating with fork&knife (0.886), chopsticks (0.899), spoon (0.820), and hand (0.787). The detection of eating with hand has the lowest performance on all three models (0.786, 0.657, 0.626), compared to the other three eating gestures.

Fig. 11 denotes the segmental F1-score for each meal session. The results are sorted by the segmental F1-score at $k=0.1$ in descending order. All the meals have F1-score higher than 0.7 for $k=0.1$. When k is increased to 0.5, two meal sessions' F1-scores are equal to or lower than 0.7 (meal_46, meal_47). The two meals were eaten with hand.

5 DISCUSSION

The proposed radar-based food intake monitoring system obtained promising results. There are several differences between our research and Xie's research [18]. Firstly, we developed an end-to-end framework for eating behavior detection. Secondly, we evaluate our model on a much larger dataset with more participants (48 vs. 6). Thirdly, we detect the eating and drinking gestures from a dataset that contains lots of other class data, whereas Xie's approach focuses on the classification between 5 eating styles (Drinking and other classes are not reported in their data.).

Currently, the conventional method for activity recognition is using a sliding-window. For each window, there is only one label. For real-life continuous eating and drinking gesture detection, the duration of food intake gestures and the time distance between two food intake gestures varies greatly (see Table 4). It is difficult to annotate the window as eating, drinking or other, because it is possible that one window can contain multiple short eating gestures, or only a part of one long eating gesture, or one eating gesture and one drinking gesture. Hence we applied the more desirable seq2seq architecture to obtain frame-wise predictions. In this way, frame-wise labels can be used in the training process, the seq2seq architecture can also enable the ability of segmentation for eating and drinking gestures.

In this research, three seq2seq models were implemented to evaluate the performance, namely the CNN-LSTM, the CNN-BiLSTM, and the proposed 3D-TCN. The 8-fold cross

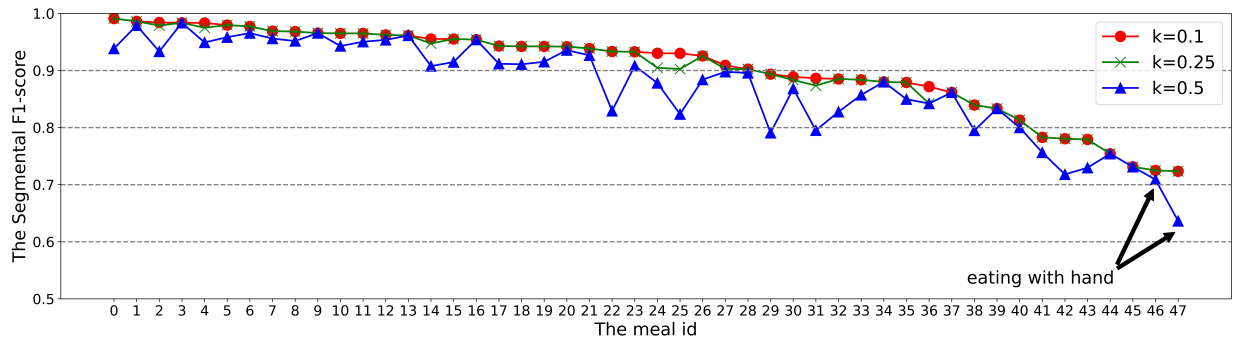


Fig. 11. The line plot of the results from 48 meals. The meal id is sorted by the segmental F1-score at $k=0.1$ in descending order. The last two meals were eaten with hand.

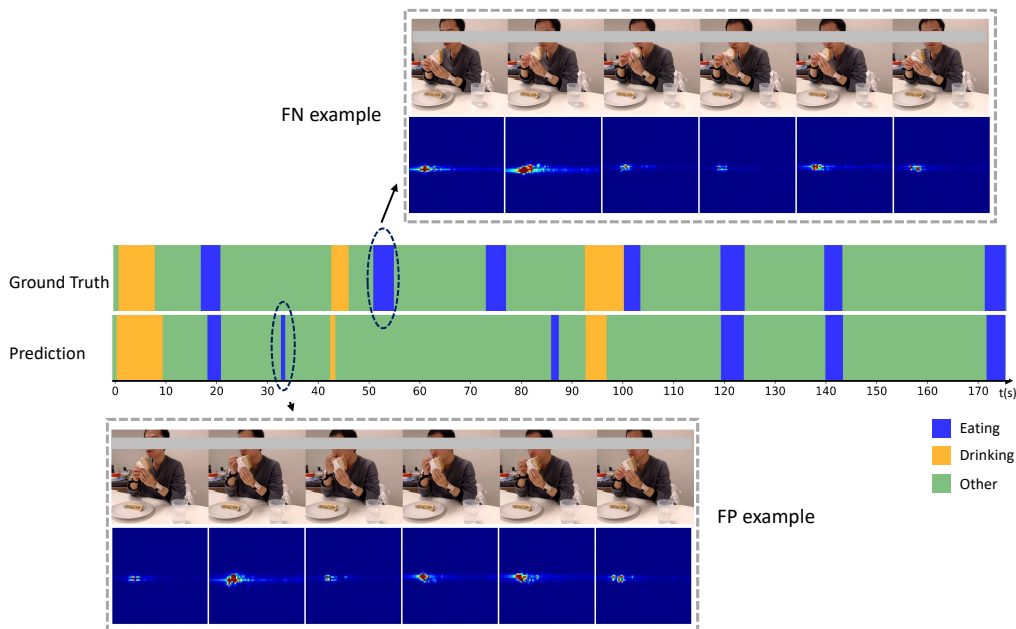


Fig. 12. Examples of the ground truth and predictions from 3D-TCN model for meal_47 in Fig. 11. In the FP example, the participant uses his right hand to touch nose while using the left hand to hold the sandwich. This movement is similar to delivering food to mouth by hand. In the FN example, the participant rotates his wrists to eat food without obvious arm and body movement.

validation results show that CNN-BiLSTM performs better than normal CNN-LSTM. Whereas the proposed 3D TCN outperforms both the CNN-LSTM model and the CNN-BiLSTM model. Meanwhile, the 3D-TCN model contains much fewer parameters than CNN-BiLSTM.

Two different radar data representations are evaluated. The performance of using RD Cube data is higher than that of using DT map data for CNN-LSTM, CNN-BiLSTM, and TCN (2D/3D), respectively. This result is consistent with our hypothesis in Section III-C, which suggests that the range information between head and hand is an important feature for radar-based food intake detection.

The performance of drinking gesture detection is lower than that of eating gesture detection. We think it is because the amount of drinking gestures is much less than that of eating gestures (608 vs 3121). The eating gestures contain four different eating styles: fork&knife, chopsticks, spoon, and hand (1232:1349:256:284). The detection performance for the gesture of eating with hand is the lowest on all three models. One potential reason is that there is more

variety for the gestures of eating with hands. Moreover, by investigating the misclassification of 3D-TCN, we found that 3.17% of the gestures belonging to eating with hand were predicted as drinking, which is higher than the other three eating gestures (0.16% for fork&knife, 0.44% for chopsticks, 1.17% for spoon). This observation suggests that the gesture of eating with hand is similar to the drinking gesture.

We investigated the meal session that obtains lowest F1-score (meal_47 in Fig.11) by checking the video, ground truth value, and the prediction. Fig. 12 shows a 3 min segment from meal_47. Two typical wrong cases are selected. For the FP example, the participant uses one hand to touch his nose, while using the other hand to hold the sandwich close to mouth. This movement is similar to eating sandwich with hand. For the FN example, the participant mainly use wrists to rotate the sandwich to his mouth, no obvious hand/arm movement is observed.

Using a FMCW radar for food intake monitoring has not been explored broadly. We propose this method as a good supplement to existing approaches such as smartwatch-

based and video-based monitoring. One application scenario is in-door activity recognition, since video monitoring at home has higher privacy concern and people could not wear a smartwatch all the time. Apart from food intake monitoring solely, this method can also be explored to monitor and assess upper limbs tremors of the elderly continuously and unobtrusively in real-life meal sessions [33].

We collected the dataset at the university, not in a home-like environment (house/apartment). However, since we applied static object removal, the stationary layout information is removed in the pre-processing step. The results on the data collected in seven different rooms with different layouts indicate that the proposed method can detect eating gestures in different environments.

However, there are still several limitations in this research. Firstly, the data were collected in static environments, which means there are no other moving objects/subjects in the FOV of radar during data collection; this is still an open problem for the current radar-based HAR research community. The performance in environments containing moving objects and persons still needs to be further explored. Secondly, the radar is deployed on the dinner table in front of the participant, although this is the easiest and the most convenient setup, more radar deployment positions are worthwhile to be explored and tested for fine-grained eating/drinking gesture detection.

6 CONCLUSION

In this research, we proposed Eat-Radar, a continuous food intake detection system, using a FMCW radar sensor and a seq2seq 3D-TCN model. The detection and segmentation of eating and drinking gestures were realized by processing RD Cube data from the radar. The effectiveness of this approach is validated on a collected dataset containing 48 meal sessions. The proposed 3D-TCN outperforms the CNN-LSTM model and the CNN-BiLSTM model both in detecting eating and drinking gestures using 8-fold cross-validation. The proposed seq2seq 3D-TCN model and the corresponding segment-wise evaluation method has the potential to be applied in other radar-based HAR research. In the future, we plan to validate our approach in a real home-like environment and over a longer time period.

ACKNOWLEDGMENT

The authors would like to thank the participants who participated in the experiments for their efforts and time. This project is funded in part by KU Leuven under grant C3/20/016, in part by Goodbrother project (Network on Privacy-Aware Audio- and Video-Based Applications for Active and Assisted Living with COST action 19121), and in part by the China Scholarship Council (CSC) under grant 202007650018.

REFERENCES

- [1] "Obesity and overweight." <https://www.who.int/news-room/fact-sheets/detail/obesity-and-overweight> (accessed Jun. 05, 2022).
- [2] L. M. Donini et al., "Malnutrition in elderly: Social and economic determinants," *J. Nutr. Heal. Aging*, vol. 17, no. 1, pp. 9–15, 2013.
- [3] W. H. Organization, *Obesity: Preventing and Managing the Global Epidemic*. Report of a WHO consultation. Geneva: World Health Organization, 2000.
- [4] P. V. Rouast and M. T. P. Adam, "Single-Stage Intake Gesture Detection Using CTC Loss and Extended Prefix Beam Search," *IEEE J. Biomed. Heal. Informatics*, vol. 25, no. 7, pp. 2733–2743, 2021.
- [5] P. V. Rouast and M. T. P. Adam, "Learning Deep Representations for Video-Based Intake Gesture Detection," *IEEE J. Biomed. Heal. Informatics*, vol. 24, no. 6, pp. 1727–1737, 2020.
- [6] J. Qiu, F. P. W. Lo, S. Jiang, Y. Y. Tsai, Y. Sun, and B. Lo, "Counting Bites and Recognizing Consumed Food from Videos for Passive Dietary Monitoring," *IEEE J. Biomed. Heal. Informatics*, vol. 25, no. 5, pp. 1471–1482, 2021.
- [7] K. Kyritsis, C. Diou, and A. Delopoulos, "A Data Driven End-to-End Approach for In-the-Wild Monitoring of Eating Behavior Using Smartwatches," *IEEE J. Biomed. Heal. Informatics*, vol. 25, no. 1, pp. 22–34, 2020.
- [8] A. Doulah, T. Ghosh, D. Hossain, M. H. Imtiaz, and E. Sazonov, "'Automatic Ingestion Monitor Version 2' - A Novel Wearable Device for Automatic Food Intake Detection and Passive Capture of Food Images," *IEEE J. Biomed. Heal. Informatics*, vol. 25, no. 2, pp. 568–576, 2021.
- [9] K. S. Lee, "Joint Audio-Ultrasound Food Recognition for Noisy Environments," *IEEE J. Biomed. Heal. Informatics*, vol. 24, no. 5, pp. 1477–1489, 2020.
- [10] G. Mertes, L. Ding, W. Chen, H. Hallez, J. Jia, and B. Vanrumste, "Measuring and Localizing Individual Bites Using a Sensor Augmented Plate during Unrestricted Eating for the Aging Population," *IEEE J. Biomed. Heal. Informatics*, vol. 24, no. 5, pp. 1509–1518, 2020.
- [11] M. P. Lasschuijt, E. Brouwer-Brolsma, M. Mars, E. Siebelink, E. Feskens, K. de Graaf and G. Camps, "Concept Development and Use of an Automated Food Intake and Eating Behavior Assessment Method," *J. Vis. Exp.* (168), e62144.
- [12] B. Zhou et al., "Smart Table Surface: A Novel Approach to Pervasive Dining Monitoring," 2015 IEEE Int. Conf. Pervasive Comput. Commun. Smart, pp. 155–162, 2015.
- [13] H. Zhao, "A Noncontact Breathing Disorder Recognition System Using 2.4-GHz Digital-IF Doppler Radar," *IEEE J. Biomed. Heal. Informatics*, vol. 23, no. 1, pp. 208–217, 2019.
- [14] J. Maitre, K. Bouchard, and S. Gaboury, "Fall Detection with UWB Radars and CNN-LSTM Architecture," *IEEE J. Biomed. Heal. Informatics*, vol. 25, no. 4, pp. 1273–1283, 2021.
- [15] F. Luo, S. Poslad, and E. Bodanese, "Kitchen Activity Detection for Healthcare using a Low-Power Radar-Enabled Sensor Network," *IEEE Int. Conf. Commun.*, 2019, pp. 1–7.
- [16] A. Gorji, T. Gielen, M. Bauduin, H. Sahli, and A. Bourdoux, "A Multi-radar Architecture for Human Activity Recognition in Indoor Kitchen Environments," 2021 IEEE Radar Conf., 2021, pp. 1–6.
- [17] J. Maitre, K. Bouchard, C. Bertuglia, and S. Gaboury, "Recognizing activities of daily living from UWB radars and deep learning," *Expert Syst. Appl.*, vol. 164, no. 113994, 2021.
- [18] Y. Xie, R. Jiang, X. Guo, Y. Wang, J. Cheng, and Y. Chen, "mmEat: Millimeter wave-enabled environment-invariant eating behavior monitoring," *Smart Heal.*, vol. 23, no. 100236, 2022.
- [19] Y. Wu, Y. Chen, S. Shirmohammadi, and C. Hsu, "AI-Assisted Food Intake Activity Recognition Using 3D mmWave Radars," In Proceedings of the 7th International Workshop on Multimedia Assisted Dietary Management (MADiMa '22). Oct, 2022, pp. 81–89.
- [20] S. Zhu, R. G. Guendel, G. S. Member, A. Yarovoy, F. Fioranelli, and S. Member, "Continuous Human Activity Recognition With Distributed Radar Sensor Networks and CNN-RNN Architectures," *IEEE Trans. Geosci. Remote Sens.*, vol. 60, pp.1–15, 2022.
- [21] M. Piriyahtakonkij et al., "SleepPoseNet: Multi-View Learning for Sleep Postural Transition Recognition Using UWB," *IEEE J. Biomed. Heal. Informatics*, vol. 25, no. 4, pp. 1305–1314, 2021.
- [22] Z. Ni and B. Huang, "Gait-Based Person Identification and Intruder Detection Using mm-Wave Sensing in Multi-Person Scenario," *IEEE Sens. J.*, vol. 22, no. 10, pp. 9713–9723, 2022.
- [23] B. Vandersmissen et al., "Indoor Person Identification Using a Low-Power FMCW Radar," *IEEE Trans. Geosci. Remote Sens.*, vol. 56, no. 7, pp. 3941–3952, 2018.
- [24] H. Sloetjes and P. Wittenburg, "Annotation by category - ELAN and ISO DCR," In Proc. 6th Int. Conf. Lang. Resour. Eval. Lr., 2008, pp. 816–820.

- [25] C. Lea, M. D. Flynn, R. Vidal, A. Reiter, and G. D. Hager, "Temporal convolutional networks for action segmentation and detection," In Proc. 30th IEEE Conf. Comput. Vis. Pattern Recognition (CVPR), 2017, pp. 1003–1012.
- [26] B. Filtjens, P. Ginis, A. Nieuwboer, P. Slaets, and B. Vanrumste, "Automated freezing of gait assessment with marker-based motion capture and multi-stage spatial-temporal graph convolutional neural networks," *J. Neuroeng. Rehabil.*, vol. 19, no. 1, pp. 1–14, 2022.
- [27] D. Jarrett, J. Yoon, and M. Van Der Schaar, "Dynamic Prediction in Clinical Survival Analysis Using Temporal Convolutional Networks," *IEEE J. Biomed. Heal. Informatics*, vol. 24, no. 2, pp. 424–436, Feb. 2020.
- [28] C. Wang, T. S. Kumar, W. De Raedt, G. Camps, H. Hallez, and B. Vanrumste, "Drinking Gesture Detection Using Wrist-Worn IMU Sensors with Multi-Stage Temporal Convolutional Network in Free-Living Environments," *Proc. Annu. Int. Conf. IEEE Eng. Med. Biol. Soc. (EMBC)*, 2022, pp. 1778–1782.
- [29] S. Bai, J. Z. Kolter, and V. Koltun, "An Empirical Evaluation of Generic Convolutional and Recurrent Networks for Sequence Modeling," 2018, [Online]. Available: <http://arxiv.org/abs/1803.01271>.
- [30] R. Xue and X. Bai, "2D-Temporal Convolution for Target Recognition of SAR Sequence Image," 2019 6th Asia-Pacific Conf. Synth. Aperture Radar, APSAR 2019, pp. 2–5.
- [31] J. Maitre, K. Bouchard, and S. Gaboury, "Fall Detection with UWB Radars and CNN-LSTM Architecture," *IEEE J. Biomed. Heal. Informatics*, vol. 25, no. 4, pp. 1273–1283, 2021.
- [32] A. Ullah, J. Ahmad, K. Muhammad, M. Sajjad, and S. W. Baik, "Action Recognition in Video Sequences using Deep Bi-Directional LSTM with CNN Features," *IEEE Access*, vol. 6, pp. 1155–1166, 2017.
- [33] N. Gillani and T. Arslan, "Unobtrusive Detection and Monitoring of Tremors using Non-Contact Radar Sensor," *Proc. 4th Int. Conf. Bio-Engineering Smart Technol.(BioSMART)*, 2021, pp. 1–4.